Study on Static Characteristics and Parameter Patterns of Spherical Hybrid Sliding Bearings Based on a Roundness Tester

Siqi Li[1], Yawen Fan[2,*], Jingfeng Shen[1,*]
[1]School of Mechanical Engineering, University of Shanghai for Science and Technology, Shanghai, China
[2]School of Engineering and Computing, University of Shanghai for Science and Technology, Shanghai, China
[*]Corresponding Author

Abstract: This paper presents a study on the static characteristics of spherical hybrid sliding bearings, which is a key structural component of a roundness tester. The influence of critical design parameters is analyzed to provide a theoretical basis for optimized design. A lubrication mathematical model based on spherical coordinates was established, and the Reynolds equation applicable to spherical bearings was derived. By incorporating the principle of flow conservation and a small-hole throttle model, the oil film pressure distribution was obtained using a coupled finite difference and relaxation iteration method. Based on the established lubrication model, the influence of oil supply pressure, eccentricity, throttle hole diameter, and oil film clearance on the bearing load-carrying capacity was systematically analyzed, and the corresponding underlying mechanisms were investigated. The analysis results indicate that an increase in oil supply pressure enhances the hydrostatic effect, thereby improving the bearing load-carrying capacity. An increase in eccentricity strengthens the hydrodynamic effect and leads to a significant improvement in load-bearing performance. In addition, the throttle hole diameter exhibits an optimal value that maximizes load-carrying capacity, which essentially reflects the matching relationship between throttling characteristics and return oil flow resistance. The proposed model and computational strategy offer effective support for parameter optimization and preliminary structural design of precision metrology bearings, contributing to improved measurement accuracy and reliability in advanced manufacturing.

Keywords: Spherical Hybrid Sliding Bearings; Orifice Restriction; Flow Continuity; Finite Difference Method; Conformal Transformation

1. Introduction

Spherical Hybrid Sliding Bearings (SHSBs) have been widely adopted in aerospace systems, roundness testers, gyroscopes, and other ultra-precision instruments owing to their high load capacity, superior stiffness, low frictional power loss, and excellent rotational accuracy [1]. As shown in Figure 1, a typical roundness tester is composed of SHSBs, a granite column, hydrostatic guideways, and a precision leveling and self-aligning worktable, and is utilized for the measurement of roundness, cylindricity, and coaxiality of ring-shaped or cylindrical rotating components.

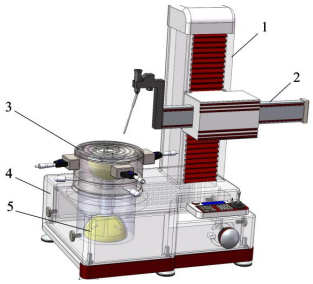

Figure 1. Roundness Tester System Structure
1-Granite column
2-Gydrostatic guideways
3-Precision leveling and self-aligning worktable
4-Granite base platform
5-SHSBs

In such measurement systems, the measurement accuracy is significantly improved by the use of SHSBs. Under the action of pressurized oil between the convex and concave spherical surfaces, the spindle is lifted and hydrodynamically supported, whereby the effects of surface machining errors, installation deviations, assembly misalignments, and slight attitude variations on the rotational accuracy of

the turntable are effectively mitigated. However, because spherical surfaces are particularly difficult to manufacture, the bearing characteristics cannot be obtained experimentally without substantially increasing development costs. Thus, numerical and simulation-based approaches are typically employed during the design stage to predict the performance of SHSBs. Although extensive numerical and simulation studies have been conducted on spherical, gas-lubricated hydrostatic bearings in recent years, research on SHSBs remains relatively limited.

In the research field of gas-lubricated spherical hydrostatic bearings, early studies established numerical approaches for solving the Reynolds equation on spherical surfaces. One representative method involved the transformation of the hemispherical surface into a rectangular plane, and the subsequent substitution of variables to render the Reynolds equation into an elliptic partial differential equation (PDE). This facilitated the calculation of gas-film pressure distributions [2]. Subsequently, hydrostatic gas-bearing models formulated in Cartesian, polar, and spherical coordinate systems were developed, and the corresponding pressure fields and load-carrying capacities were obtained by solving the governing partial differential equations. The influence of conformality on numerical accuracy and computational efficiency was systematically investigated [3]. The advent of numerical techniques has precipitated the integration of iterative algorithms with finite-difference schemes, a development that has facilitated the attainment of approximate solutions to the Reynolds equation. This, in turn, has enabled the execution of parametric studies that investigate the impact of supply pressure and restrictor orifice diameter on the bearing load capacity [4]. In order to enhance numerical precision, small-perturbation theory was amalgamated with weighted-residual methodologies, including the Galerkin method. This integration facilitated meticulous examinations of dynamic coefficients and their reliance on perturbation frequency, eccentricity, and structural parameters [5]. Furthermore, the steady-state load capacity and dynamic characteristics of hemispherical spiral-groove hybrid gas bearings were investigated, revealing the influence of groove geometry on bearing performance [6]. Furthermore, the cavitation phenomena manifesting in spherical bearings were contemplated, with concomitant analyses of film pressure, elastic deformation, and load capacity undertaken utilising finite-element methods [7].

In the research area of SHSBs, early numerical modelling employed triangular finite elements with linear interpolation functions to describe the lubrication film, thereby establishing the foundation for finite-element analysis of spherical bearing lubrication problems [8]. Subsequent studies have derived pressure distributions and fluid-film thickness expressions for hemispherical shells under arbitrary orientations, including horizontal configurations. These studies have also proposed modified formulations for film-thickness calculation [9]. Subsequent incorporation of the centrifugal effects induced by spherical geometries into lubrication analyses yielded analytical pressure solutions through Sommerfeld-type transformations, thereby providing significant theoretical underpinnings for the optimisation and design of spherical bearings [10]. In more recent studies, dynamic lubrication equations under laminar-flow conditions have been derived using small-perturbation methods, and numerical analyses of spherical bearing operating characteristics have been performed by unfolding the bearing surface and establishing analogies with journal bearing models [11].

This study builds upon the extant literature by investigating a SHSBs and developing a numerical lubrication model for its performance analysis. The hemispherical surface is unfolded into a rectangular plane, discretised, and solved using the finite-difference method to obtain the pressure distribution from the transformed Reynolds equation. The subsequent evaluation encompasses the impact of initial film thickness, supply pressure, and orifice diameter on the bearing's load capacity and stiffness.

2. Operating Principle and Numerical Modeling of SHSBs

2.1 Operating Principle

The shaft system of SHSBs comprises a hydraulic oil supply system, a cooling system, two hemispherical bearing surfaces, and a spindle, as illustrated in Figure 2. The bearing is formed by the mating of a convex and a concave hemispherical surface. The convex sphere (4) functions as the bearing rotor and is equipped with multiple supply orifices, while the concave sphere (3) serves as the bearing stator and

features four hydrostatic recesses (5). During operation, the hydraulic oil supply system (6) delivers pressurised oil to these recesses, thereby generating supporting oil films within the four pockets that provide the bearing load capacity.

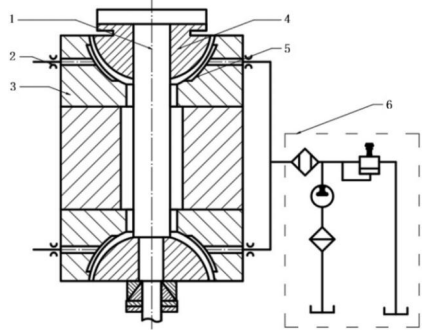

Figure 2. Structure of SHSBs Shaft System

1-Axis of rotation
2-External throttle
3-Concave hemispere
4-Convex hemisphere
5-Oil cavity
6-Oil supply system

The operating principle of a hydrostatic bearing is predicated on the continuous supply of hydraulic oil at a prescribed pressure through a throttling device into the bearing recesses. The throttling element is responsible for regulating the flow rate and establishing a pressure drop between the supply line and the recesses. This enables the formation of a stable and uniformly distributed pressurised lubricant film within the bearing clearance. The application of pressurised oil film results in the complete separation of the bearing surfaces, thereby preventing direct mechanical contact and significantly reducing friction and wear. In the context of steady operating conditions, the pressure distribution within the lubricant film generates a counterbalancing force that is effective in resisting external loads, whilst concurrently providing high stiffness and damping characteristics. Consequently, hydrostatic bearings demonstrate exceptional load-bearing capabilities, minimal frictional losses, and superior motion accuracy, rendering them especially well-suited for precision and ultra-precision mechanical systems

2.2 Numerical Modeling

The seminal work of Osborne Reynolds on lubrication theory in 1886 resulted in the formulation of the generalized Reynolds equation, as expressed in equation 1. In the spherical coordinate system, the generalized Reynolds equation is transformed into a mathematical model describing spherical bearings with the lower hemispherical shell in an arbitrary configuration [9].

$$\frac{1}{\sin\theta}\frac{\partial}{\partial\theta}\left(\sin\theta\frac{\rho h^3}{\mu}\frac{\partial p}{\partial\theta}\right)+\frac{1}{\sin^2\theta}\frac{\partial}{\partial\varphi}\left(\frac{\rho h^3}{\mu}\frac{\partial p}{\partial\varphi}\right) = 6R^2\cdot\left[\omega\cos\beta\sin\varphi\frac{\partial(\rho h)}{\partial\theta}+(\omega\sin\beta+\omega\cos\beta\frac{\cos\theta}{\sin\theta}\cos\varphi)\frac{\partial(\rho h)}{\partial\varphi}+2\frac{\partial(\rho h)}{\partial t}\right] \quad (1)$$

Assuming the lubricant is an incompressible fluid, it can be demonstrated that the density, denoted by ρ, can be eliminated from both sides of the equation. In circumstances where the flow velocity is sufficiently low, the lubrication process may be regarded as steady, and thus all time-dependent terms may be omitted. Furthermore, when the bearing is in a horizontal position, the half-inclination angle is $\beta = 90°$, whereby the above equation can be simplified to the following form:

$$\sin\theta\frac{\partial}{\partial\theta}\left(\sin\theta\cdot h^3\frac{\partial p}{\partial\theta}\right)+\frac{\partial}{\partial\varphi}\left(h^3\frac{\partial p}{\partial\varphi}\right)=0 \quad (2)$$

For computational convenience, equation 2 is nondimensionalized by introducing $\theta = \frac{360\Theta}{2\pi}$, $\varphi = \frac{360\Phi}{2\pi}$, $h = h_0 H$, $p = p_a P$.

Substituting these relations into equation 2, the nondimensional Reynolds equation for a spherical hydrostatic sliding bearing is obtained as follows:

$$\sin\Theta\frac{\partial}{\partial\Theta}\left(\sin\Theta H^3\frac{\partial P}{\partial\Theta}\right)+\frac{\partial}{\partial\Phi}\left(H^3\frac{\partial P}{\partial\Phi}\right)=0 \quad (3)$$

It is evident that the introduction of an eccentric offset is a consequence of two factors: the bearing's self-weight and the externally applied load. This results in a non-uniform oil-film thickness in all directions. Accordingly, the oil-film thickness of a hemispherical shell oriented arbitrarily can be expressed as follows:

$$h = h_0 + e_r(\cos\varphi\sin\theta\sin\beta+\cos\beta\cos\theta) - e_z(\cos\varphi\sin\theta\cos\beta-\cos\theta\sin\beta) \quad (4)$$

The bearing is assumed to be in the horizontal position, as illustrated in Figure 3.

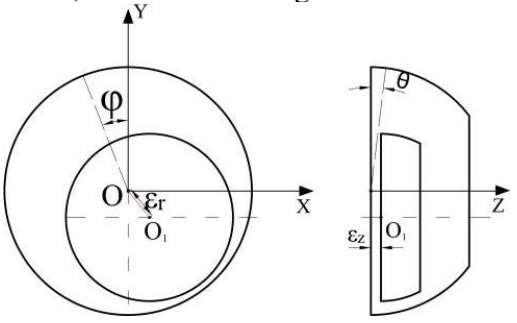

Figure 3. Spherical Coordinate System Eccentricity

Substitution of the following equations into equation 4 is required: $\beta = 90^{\circ}$, $\theta = \frac{360\Theta}{2\pi}$, $\varphi = \frac{360\Phi}{2\pi} h = h_0 H$, $e_r = h_0\varepsilon_r$, $e_z = h_0\varepsilon_z$.

$$H = 1 + \varepsilon_r cos\Phi sin\Theta + \varepsilon_z cos\Theta \quad (5)$$

3. The Simplified Mathematical Transformation of Spherical Bearing

3.1 Conformal Transformation

At present, there are two general approaches that are commonly utilised in order to solve the Reynolds equation for spherical bearings. The first method is to solve the equation directly using the finite-difference method. The second approach involves the unfolding of the spherical surface onto a rectangular plane. However, due to the disparity in spatial curvature between the sphere and the plane, direct mapping of the spherical surface onto a plane engenders local stretching or compression of specific regions. Consequently, a conformal transformation is imperative to maintain curvature and ensure geometric consistency during the mapping process. Therefore, the following is established: $\alpha = -ln tan(\theta/2)$. It follows that $sin\theta = \frac{2e^{\alpha}}{1+e^{2\alpha}}$, $\frac{d\theta}{d\alpha} = -sin\theta$.

Substituting these relations into equation 3 and equation 5 yields:

$$\frac{\partial}{\partial\alpha}\left(H^3\frac{\partial P}{\partial\alpha}\right) + \frac{\partial}{\partial\Phi}\left(H^3\frac{\partial P}{\partial\Phi}\right) = 0 \quad (6)$$

$$H = 1 + \varepsilon_r cos\Phi\frac{2e^{\alpha}}{1+e^{2\alpha}} + \varepsilon_z\frac{e^{2\alpha}-1}{1+e^{2\alpha}} \quad (7)$$

3.2 Mesh Generation and Boundary Conditions

3.2.1 Mesh generation

Subsequent to the conformal transformation, the lubricating-film domain on the original spherical surface is mapped onto a rectangular plane, as illustrated in Figure 4. The upper and lower boundaries correspond to ambient-pressure boundaries, with the pressure fixed at standard atmospheric pressure. The left and right boundaries are generated from the same meridian of the spherical surface; therefore, periodic boundary conditions are applied, thereby ensuring equal pressure values on the two sides.

The total number of grid nodes thus generated is 300×150, which equates to 45,000. Of these, $298 \times 148 = 44{,}104$ are classified as internal nodes. Each internal grid node is associated with an unknown pressure value Pi, j, resulting in one finite-difference equation per node. Consequently, the total number of algebraic equations constituting the nonlinear equation system to be solved is 44,104. The relaxation factor employed is 0.5, and the system is solved using an iterative relaxation scheme until convergence. This process yields the pressure field $P_{i,j}$ and the corresponding film-thickness distribution H_i at each node. The pressure distribution over the entire load-carrying region of the bearing can then be obtained from these values.

3.2.2 Boundary conditions

The working mechanism of the SHSBs is the basis for the following explanation. The upper and lower ends of the bearing act as discharge boundaries which are directly connected to the external environment. Consequently, the pressure at these boundaries is prescribed as the standard atmospheric pressure.

Dimensional $P(\alpha_1, \varphi) = P(\alpha_2, \varphi) = P_a$ (8)

Dimensionless $P(\alpha_1, \Phi) = P(\alpha_2, \Phi) = 1$ (9)

In the unfolded rectangular domain, the left and right boundaries originate from the same generatrix of the spherical surface. Accordingly, periodic boundary conditions are applied to ensure continuity of pressure across these two edges.

$$P(\Phi) = P(\Phi + 2\pi) \quad (10)$$

The pressure distribution surrounding the restrictor outlet is specified according to the mass-conservation condition, which equates the inflow and outflow through the throttling orifice.

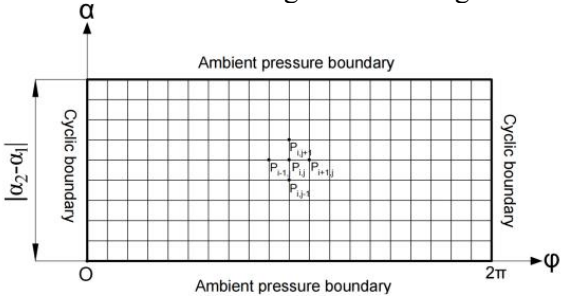

Figure 4. Meshing and Boundary Conditions

3.3 Iterative Computation of the Finite-Difference Form of the Reynolds Equation

Equation 6 is a second-order nonlinear partial differential equation, for which an analytical solution is extremely difficult to obtain. Therefore, numerical methods are employed to approximate the solution to this equation. The governing equation is first discretised into a finite-difference form, and the oil-film pressure distribution is subsequently computed using a relaxation or successive over-relaxation (SOR) iterative scheme [12]. The Reynolds equation is

formulated in the standard form of a second-order partial differential equation 11:

$$A\frac{\partial^2 P}{\partial \alpha^2} + B\frac{\partial^2 P}{\partial \Phi^2} + C\frac{\partial P}{\partial \alpha} + D\frac{\partial P}{\partial \Phi} = E \tag{11}$$

From equation 6, expanding and simplifying the expression yields equation 12.

$$H^3\frac{\partial^2 P}{\partial \alpha^2} + H^3\frac{\partial^2 P}{\partial \Phi^2} + 3H^2\frac{\partial H}{\partial \alpha}\frac{\partial P}{\partial \alpha} + 3H^2\frac{\partial H}{\partial \Phi}\frac{\partial P}{\partial \Phi} = 0 \tag{12}$$

by applying the central difference formula and substituting equation 13 and 14 to equation 12 into equation 15.

$$\begin{cases} A(\alpha, \Phi) = \left(1 + \varepsilon_r \cos\Phi \frac{2e^{\alpha}}{1+e^{2\alpha}} + \varepsilon_z \frac{e^{2\alpha}-1}{1+e^{2\alpha}}\right)^3, \\ B(\alpha, \Phi) = \left(1 + \varepsilon_r \cos\Phi \frac{2e^{\alpha}}{1+e^{2\alpha}} + \varepsilon_z \frac{e^{2\alpha}-1}{1+e^{2\alpha}}\right)^3, \\ C(\alpha, \Phi) = 3\left(1 + \varepsilon_r \cos\Phi \frac{2e^{\alpha}}{1+e^{2\alpha}} + \varepsilon_z \frac{e^{2\alpha}-1}{1+e^{2\alpha}}\right)^2, \\ D(\alpha, \Phi) = 3\left(1 + \varepsilon_r \cos\Phi \frac{2e^{\alpha}}{1+e^{2\alpha}} + \varepsilon_z \frac{e^{2\alpha}-1}{1+e^{2\alpha}}\right)^2 \\ \qquad \times \left(-\varepsilon_r \sin\Phi \frac{2e^{\alpha}}{1+e^{2\alpha}}\right), \\ E(\alpha, \Phi) = 0 \end{cases} \tag{13}$$

$$\begin{cases} \left(\frac{\partial P}{\partial \alpha}\right)_{i,j} = \frac{P_{i+1,j} - P_{i-1,j}}{2\Delta\alpha}, \\ \left(\frac{\partial P}{\partial \Phi}\right)_{i,j} = \frac{P_{i,j+1} - P_{i,j-1}}{2\Delta\Phi}, \\ \left(\frac{\partial^2 P}{\partial \alpha^2}\right)_{i,j} = \frac{P_{i+1,j} + P_{i-1,j} - 2P_{i,j}}{(\Delta\alpha)^2}, \\ \left(\frac{\partial^2 P}{\partial \Phi^2}\right)_{i,j} = \frac{P_{i,j+1} + P_{i,j-1} - 2P_{i,j}}{(\Delta\Phi)^2} \end{cases} \tag{14}$$

$$\begin{aligned} &A(\alpha_i, \Phi_j)\frac{P_{i,j+1} - 2P_{i,j} + P_{i,j-1}}{(\Delta\alpha)^2} \\ &+B(\alpha_i, \Phi_j)\frac{P_{i+1,j} - 2P_{i,j} + P_{i-1,j}}{(\Delta\Phi)^2} \\ &+C(\alpha_i, \Phi_j)\frac{P_{i,j+1} - P_{i,j-1}}{2\Delta\alpha} \\ &+D(\alpha_i, \Phi_j)\frac{P_{i+1,j} - P_{i-1,j}}{2\Delta\Phi} = 0 \end{aligned} \tag{15}$$

After collecting like terms, the following expression is obtained equation 16:

$$\begin{aligned} P_{i,j} = &\frac{1}{4}\{\Delta\Phi^2\left[2A(\alpha_i, \Phi_j) + \Delta\Phi B(\alpha_i, \Phi_j)\right]P_{i,j+1} \\ &+\Delta\Phi^2\left[2A(\alpha_i, \Phi_j) - \Delta\Phi B(\alpha_i, \Phi_j)\right]P_{i,j-1}\} \\ &/\left[\left(\frac{2e^{\alpha}}{1+e^{2\alpha}}\Delta\alpha\right)^2 A(\alpha_i, \Phi_j) + \Delta\Phi^2 C(\alpha_i, \Phi_j)\right] \\ &+\frac{1}{4}\left\{\left[2C(\alpha_i, \Phi_j) - \frac{2e^{\alpha}}{1+e^{2\alpha}}\Delta\alpha D(\alpha_i, \Phi_j)\right]P_{i+1,j}\right. \\ &\left.+\left[2C(\alpha_i, \Phi_j) + \frac{2e^{\alpha}}{1+e^{2\alpha}}\Delta\alpha D(\alpha_i, \Phi_j)\right]P_{i-1,j}\right\} \\ &/\left[\left(\frac{2e^{\alpha}}{1+e^{2\alpha}}\Delta\alpha\right)^2 A(\alpha_i, \Phi_j) + \Delta\Phi^2 C(\alpha_i, \Phi_j)\right] \end{aligned} \tag{16}$$

By enforcing the discretized equations at every node, the dependence of the nodal pressure $P_{i,j}$ on the pressures of the adjacent nodes can be determined [13] equation 17.

$$\begin{aligned} \widetilde{P}_{i,j}^{k} = &C_N P_{i,j+1}^{k} + C_S P_{i,j-1}^{k+1} + C_E P_{i+1,j}^{k} \\ &+ C_W P_{i-1,j}^{k+1} + G \end{aligned} \tag{17}$$

Where C_N, C_S, C_E, C_W, G are equation 18

$$\begin{cases} C_N = \frac{\left(\frac{B}{\Delta\Phi^2} + \frac{D}{2\Delta\Phi}\right)}{K}, \\ C_S = \frac{\left(\frac{B}{\Delta\Phi^2} - \frac{D}{2\Delta\Phi}\right)}{K}, \\ C_E = \frac{\left(\frac{A}{\Delta\alpha^2} + \frac{C}{2\Delta\alpha}\right)}{K}, \\ C_W = \frac{\left(\frac{A}{\Delta\alpha^2} - \frac{C}{2\Delta\alpha}\right)}{K}, \\ G = -\frac{E}{K}, \\ K = 2\left(\frac{A}{\Delta\alpha^2} + \frac{B}{\Delta\Phi^2}\right) \end{cases} \tag{18}$$

The pressures indicated by the superscript k correspond to the previous (uncorrected) iteration values, whereas the superscript $k+1$ represents the corrected pressures that are employed in the subsequent iteration.

To enhance the stability and convergence of the iteration, relaxation or successive over-relaxation techniques are typically adopted as shown in equation 19. Specifically, the new pressure value $P_{i,j}^{k+1}$ is formed by weighting and combining the old value $P_{i,j}^{k}$ with the newly calculated pressure, and this corrected value is subsequently used for the convergence check and for the next iteration step.

$$P_{i,j}^{k+1} = (1 - \alpha_k)P_{i,j}^{k} + \alpha_k \widetilde{P}_{i,j}^{k} \tag{19}$$

The relaxation parameter α_k is a positive scalar, generally chosen to be less than unity. In the present work, a value of 0.5 is adopted.

Because the iterative pressure update is formed by combining the previously stored and newly computed nodal pressures, the intermediate pressure values do not exactly satisfy equation 20. However, the iterative process converges to the correct solution. Convergence is determined using a relative-error criterion, with the tolerance set to $\varepsilon = 0.0001$.

Relative tolerance–based convergence criterion:

$$\frac{\sum_{i=1}^{m}\sum_{j=1}^{n}\left|P_{i,j}^{k+1} - P_{i,j}^{k}\right|}{\sum_{i=1}^{m}\sum_{j=1}^{n}P_{i,j}^{k+1}} \le \varepsilon \tag{20}$$

4. Orifice Flow-Rate Computation and Flow Equilibrium Condition

4.1 Computation of the Inflow Rate through the Capillary Orifice

In SHSBs, the flow characteristics of the throttling element play a critical role in establishing the pressure within the recesses and, consequently, in determining the load-carrying capacity and static performance of the bearing. To describe the flow behaviour of the lubricant

supplied to the recesses under a prescribed supply pressure, a flow-rate model based on the assumptions of incompressible fluid flow and energy conservation is commonly employed. Accordingly, the inflow rate through the capillary orifice can be expressed as a function of the pressure difference between the supply line and the recess, as given by the following equation 21:

$$Q_{in} = \alpha \frac{\pi {d_0}^2}{4} \sqrt{\frac{2(P_S - P_R)}{\rho_t}} \quad (21)$$

Here, $\alpha = 0.6 \sim 0.8$ is the flow coefficient; $d_0 = 4.0 \times 10^{-3} m$ is the orifice diameter; $\rho_t = 870\, kg/m^3$ is the lubricant density; $P_s = 20 \times 10^5 Pa$ is the supply pressure; and P_R denotes the oil-chamber pressure.

The orifice diameter is transformed into equation 22 and equation 23:

$$d_{Hmax} = \left| ln\left(1 - \frac{d_0}{2Rtan\left(\frac{\theta_d}{2}\right)}\right)\right| \quad (22)$$

$$d_{Hmin} = \left| ln\left(1 + \frac{d_0}{2Rtan\left(\frac{\theta_d}{2}\right)}\right)\right| \quad (23)$$

Because the calculated d_{Hmax} and d_{Hmin} values are very close to each other, it is sufficient to select either one.

4.2 Flow Rate Calculation at a Small Orifice Throttle

Figure 5 illustrates the flow-control model of the spherical hydrostatic pocket. High-pressure oil is supplied through the central orifice, generating the supply pressure P_s and the inflow rate Q_n. Driven by the cavity pressure, the lubricant spreads circumferentially along the spherical clearance and leaks from the four boundaries of the pocket, namely ab, bc, cd, and da, resulting in the corresponding leakage flows Q_{ab}, Q_{bc}, Q_{cd}, and Q_{da}. The orifice exit pressure is determined from the flow-conservation principle, wherein the inflow through the orifice equals the total outflow from the control region.

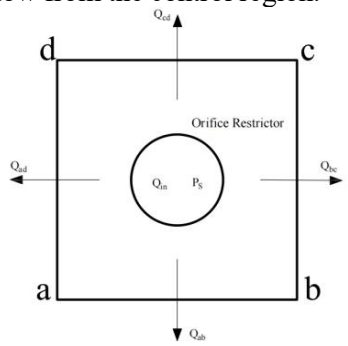

Figure 5. Flow-Control Model of the Spherical Hydrostatic Oil Chambe

4.2.1 Calculation of circumferential flow rate

Based on the classical lubrication theory and under the assumptions of laminar flow and negligible inertia effects, the circumferential flow rate per unit width can be expressed as a function of the local film thickness and the circumferential pressure gradient, as given by the following equation 24 and equation 25:

$$q_\varphi = -\frac{h^3}{12\mu r sin\theta}\left(\frac{\partial p}{\partial \varphi}\right) \quad (24)$$

Let $\alpha = -lntan(\theta/2)$, $sin\theta = \frac{2e^\alpha}{1+e^{2\alpha}}$, $\frac{d\theta}{d\alpha} = -sin\theta$

$$\begin{aligned} Q_\varphi &= -\int_{\frac{\sqrt{2}}{6}}^{\frac{\pi}{2}} \frac{h^3}{12\mu r \sin\theta}\left(\frac{\partial p}{\partial \varphi}\right) d\theta \\ &= -\int_{a_1}^{a_2} \frac{h_0^3 p_a}{12\mu R} \cdot H^3 \cdot \frac{\partial P}{\partial \Phi} d\alpha \end{aligned} \quad (25)$$

Nondimensional circumferential flow rate $\overline{Q_\varphi} = \frac{12\mu R}{h_0^3 P_a} Q_\varphi$, therefore $\overline{Q_\varphi} = \int_{\alpha_2}^{\alpha_1} H^3 \frac{\partial P}{\partial \Phi} d\alpha$, $\alpha_1 = 1.317$, $\alpha_2 = 0$

4.2.2 Calculation of axial flow rate

Assuming laminar flow, incompressible lubricant, and negligible inertia effects, the axial flow rate per unit width can be expressed in terms of the local film thickness and the axial pressure gradient, as given by the following equation 26 and equation 27:

$$q_\theta = -\frac{h^3}{12\mu r}\frac{\partial p}{\partial \theta} \quad (26)$$

$$\begin{aligned} Q_\theta &= \int_0^{2\pi} \frac{h^3}{12\mu r}\left(\frac{\partial p}{\partial \theta}\right) d\Phi \\ &= \int_0^{2\pi} \frac{h_0^3 P_a}{12\mu R} \cdot H^3 \cdot \frac{1}{\sin\theta} \cdot \frac{\partial P}{\partial \alpha} d\varphi \\ &= \int_0^{2\pi} \frac{h_0^3 P_a}{12\mu R} \cdot H^3 \cdot \frac{1+e^{2\alpha}}{2e^\alpha} \cdot \frac{\partial P}{\partial \alpha} d\phi \end{aligned} \quad (27)$$

Nondimensional axial flow rate $\overline{Q_\theta} = \frac{12\mu R}{h_0^3 P_a} Q_\theta$, therefore $\overline{Q_\theta} = \int_0^{2\pi} H^3 \frac{1+e^{2\alpha}}{2e^\alpha}\frac{\partial P}{\partial \alpha} d\Phi$.

As shown in Figure 5, the flow rate through the orifice equals the sum of the flow rates through the four edges, which corresponds to equation 28 and equation 29.

$$Q_{out} = Q_{ab} + Q_{bc} + Q_{cd} + Q_{ad} \quad (28)$$

Substituting equation 25 and equation 27 into equation 28 yields the orifice outflow rate formula given by equation 29:

$$\begin{aligned} Q_{out} &= 2\int_0^{2\pi} \left(1 + \varepsilon_r cos\,\varphi \frac{2e^\alpha}{1+e^{2\alpha}} + \varepsilon_z \frac{e^{2\alpha}-1}{1+e^{2\alpha}}\right)^3 \\ &\times \frac{1+e^{2\alpha}}{2e^\alpha}\frac{\partial p}{\partial \alpha} d\Phi \end{aligned} \quad (29)$$

4.3 Flow Continuity Condition

According to the continuity equation and the principle of mass conservation, the mass flow rate through the orifice must be identical at the inlet and outlet under steady-state conditions

By substituting equation 17 and equation 28 into the continuity equation and simplifying, we obtain equation 30:

$$\begin{cases} Q_{in} = Q_{out}, \\ \alpha \dfrac{\pi {d_{Hmax}}^2}{4} \sqrt{\dfrac{2(P_s - P_{out})}{\rho_t}} \\ = 2\int_0^{2\pi} (1 + \varepsilon_r cos\Phi \dfrac{2e^{\alpha}}{1+e^{2\alpha}} \\ + \varepsilon_z \dfrac{e^{2\alpha}-1}{1+e^{2\alpha}})^3 \dfrac{1+e^{2\alpha}}{2e^{\alpha}} \dfrac{\partial P}{\partial \alpha} d\Phi \end{cases} \quad (30)$$

The pressure P was obtained by simultaneously solving equations 20 to equation 34, discretizing the flow-rate expressions, and applying the relaxation iteration method. The numerical solution of the static characteristics is then computed using a MATLAB program, and the corresponding workflow is shown in Figure 6.

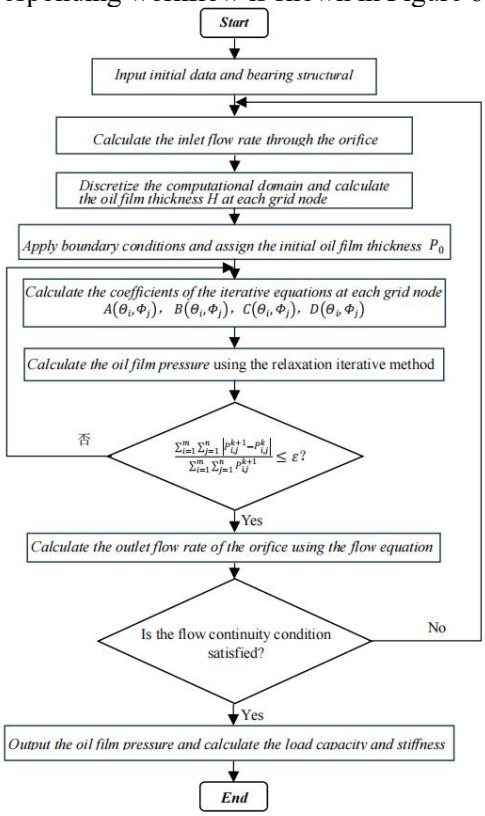

Figure 6. Oil Film Pressure Calculation program flow diagram

4.4 Evaluation of Load Capacity and Stiffness

4.4.1 Evaluation of load capacity

Dimensional form load capacity can be expressed as equation 31.

$$\begin{cases} F_x = R^2 \int_{\frac{\pi}{6}}^{\frac{\pi}{2}} sin^2\varphi d\varphi \int_0^{2\pi} (P - P_a) cos\theta d\theta \\ F_y = R^2 \int_{\frac{\pi}{6}}^{\frac{\pi}{2}} sin^2\varphi d\varphi \int_0^{2\pi} (P - P_a) sin\theta d\theta \\ F_z = R^2 \int_{\frac{\pi}{6}}^{\frac{\pi}{2}} sin\varphi d\varphi \int_0^{2\pi} (P - P_a) d\theta \end{cases} \quad (31)$$

The nondimensional form can be expressed as equation 32.

$$\begin{cases} \overline{F_x} = R^2 \int_{\frac{\pi}{6}}^{\frac{\pi}{2}} sin^2\Phi d\Phi \int_0^{2\pi} (P - P_a) cos\Theta d\Theta \\ \overline{F_y} = R^2 \int_{\frac{\pi}{6}}^{\frac{\pi}{2}} sin^2\Phi d\Phi \int_0^{2\pi} (P - P_a) sin\Theta d\Theta \\ \overline{F_z} = R^2 \int_{\frac{\pi}{6}}^{\frac{\pi}{2}} sin\Phi d\Phi \int_0^{2\pi} (P - P_a) d\Theta \end{cases} \quad (32)$$

Radial load capacity $\overline{F_r} = \sqrt{\overline{F_x}^2 + \overline{F_y}^2}$, axial load capacity F_z.

4.4.2 Evaluation of stiffness

Based on the definition of stiffness, the stiffness of the bearing can be expressed as equation $K = \frac{dW}{d\varepsilon}$, the nondimensional form can be expressed as equation 33.

$$\overline{K} = \frac{d\overline{W}}{d\varepsilon} \quad (33)$$

5. Results and Discussion

The analysis and computation presented in this work are based on SHSBs model, whose key parameters are summarized in Table 1.

Table 1. SHSBs Structure Parameters

Basic parameter	Value
Bearing radius (R/m)	0.06
Initial oil film thickness (h_0/m)	1×10^{-5},1.5×10^{-5}, 2×10^{-5}
Stator outer wrap angle (θ_o)	90°
Stator inner wrap angle (θ_i)	30°
Number of restrictor orifices (n)	4
Angular distribution of the throttling orifices (θ_1)	60°
Restrictor orifice diameter (d_0/m)	0.004
Ambient pressure (P_a/MPa)	0.1
Dynamic viscosity (η/P_a·s)	5.835×10^{-3}
Density (ρ/kg·m^{-3})	873
Circumferential eccentricity ratio(ε_r)	0,0.2,0.4,0.6,0.8
Axial eccentricity ratio (ε_z)	0,0.2,0.4,0.6,0.8
Supply pressure (P_s/MPa)	2,4,6
Half tilt angle (β)	90°

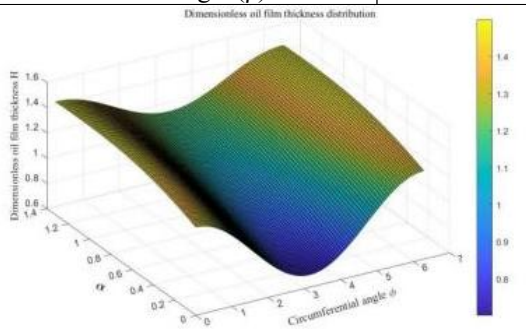

Figure 7. Dimensionless Oil Film Thickness

Figure 7 shows the nondimensional film-thickness distribution of the spherical hydrostatic bearing for $\varepsilon_r = 0.4$ and $\varepsilon_z = 0.4$. Based on this

distribution, the film thickness at each grid point is determined and subsequently used in the discretized equations to calculate the corresponding nodal pressures.

5.1 Pressure Distribution in the Bearing Oil Film

As demonstrated in Figure 8, for a supply pressure of $P_s = 2$, a circumferential eccentricity of $\varepsilon_r = 0.4$, and an axial eccentricity of $\varepsilon_z = 0.4$, the dimensionless oil-film pressure P is derived through the application of the transformation $\alpha = ln(tan(\theta/2))$ to the polar angle θ and the unfolding of the hemispherical surface onto a plane. As illustrated by the figure, the oil-film pressure undergoes a precipitous decline from each of the four restrictor orifices towards the surrounding regions.

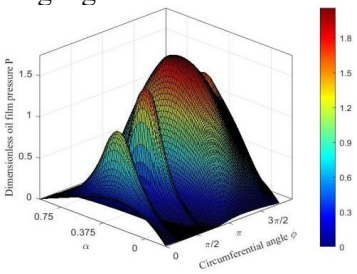

Figure 8. Dimensionless Oil Film Pressure

As illustrated in Figure 9, the dimensionless oil-film pressure distribution is presented along the 45° meridional plane under various supply pressures. The circumferential eccentricity has been fixed at $\varepsilon_r = 0.4$ and the axial eccentricity at $\varepsilon_z = 0.4$. As demonstrated, the maximum pressure is observed to occur at the restrictor orifice, with a concomitant decrease in pressure on both sides of the orifice in the circumferential direction. Furthermore, it is evident that an increase in supply pressure P_s results in a corresponding rise in dimensionless oil-film pressure.

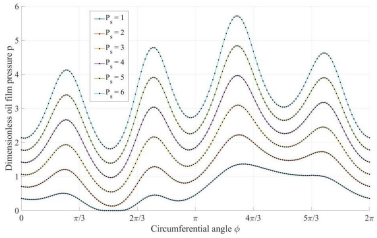

Figure 9. Dimensionless Oil Film Pressure under Different Charge Oil Pressure

5.2 Influence of the Initial Film Clearance on Bearing Performance

As illustrated by Figures 10 and 11, the relationship between the initial film clearance and the bearing load capacity (N) obtained from numerical calculations is demonstrated.

When the eccentricity is less than 0.4, the load capacity is negligible. Consequently, in the field of bearing design, it is recommended that a larger eccentricity be adopted in order to achieve higher load capacity. In a similar manner, the relationship between initial film clearance and stiffness is demonstrated in Figures 12 and 13. It is evident that $K(N)$ demonstrates a congruent trend, whereby an augmentation in eccentricity is concomitant with an increase in stiffness.

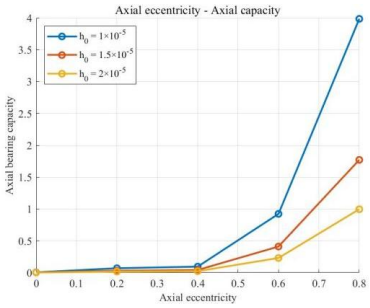

Figure 10. Axial Eccentricity - Axial Capacity

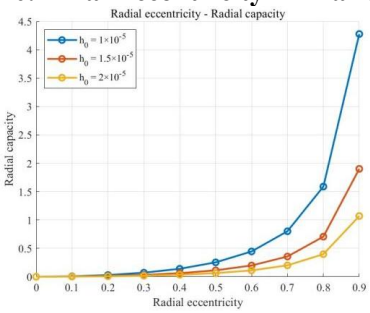

Figure 11. Radial Eccentricity - Radial Capacity

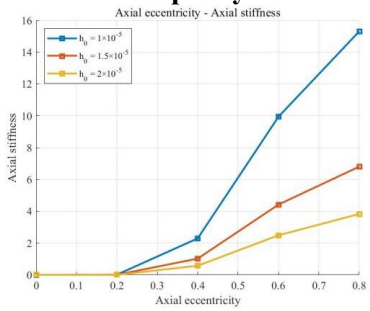

Figure 12. Axial Eccentricity - Axial Stiffness

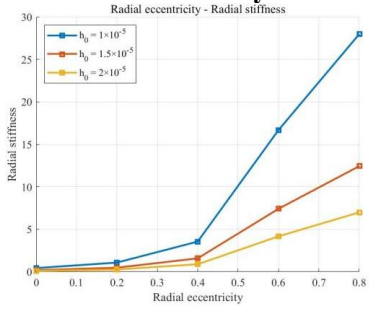

Figure 13. Radial Eccentricity - Radial Stiffness

5.3 Effect of Supply Pressure on Bearing Performance

Figures 14 and 15 present the relationship between supply pressure and the bearing load capacity obtained from numerical calculations. It is evident that the supply pressure exerts a pronounced influence on the static performance of the spherical hybrid bearing. As the supply pressure increases, both axial and radial load capacities rise significantly across all eccentricities. This is due to the formation of a stronger hydrostatic film under higher supply pressure.

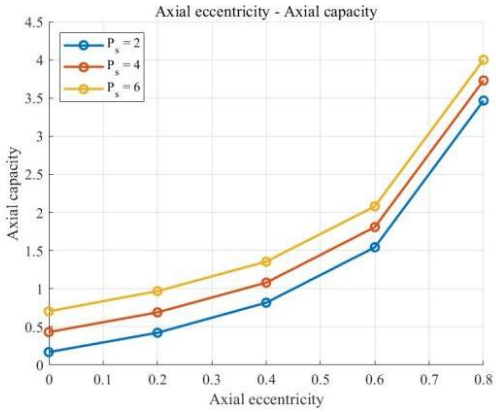

Figure 14. Axial Eccentricity - Axial Capacity

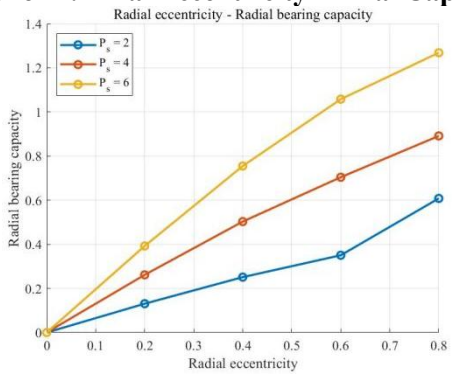

Figure 15. Radial Eccentricity - Radial Capacity

As demonstrated in Figures 16 and 17, there is a corresponding variation in film stiffness with supply pressure. The findings of the present study demonstrate that an increase in supply pressure is concomitant with an increase in film stiffness. Although the axial stiffness is known to decrease with increasing eccentricity, its absolute magnitude has been shown to consistently increase as the supply pressure rises. The radial stiffness demonstrates a more intricate relationship with eccentricity; nevertheless, an elevated supply pressure invariably results in enhanced stiffness levels under all operating conditions.

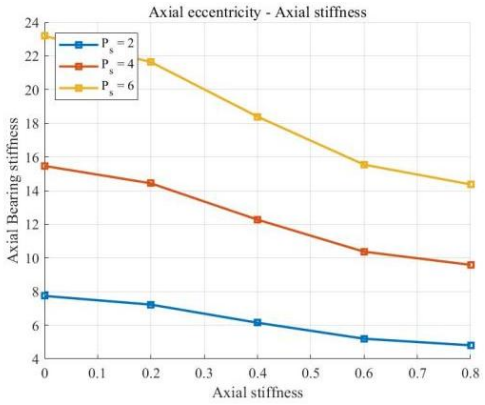

Figure 16. Axial Eccentricity - Axial Stiffness

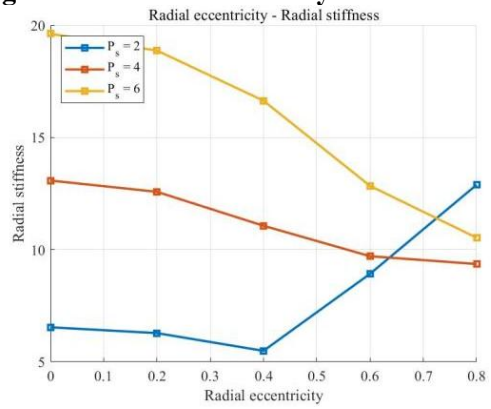

Figure 17. Radial Eccentricity - Radial Stiffness

It is evident that an increase in supply pressure has a significant impact on the load-bearing capacity and stiffness of the lubricant film. This, in turn, enhances the static performance of spherical hybrid bearings.

5.4 Effect of Orifice Diameter on Bearing Performance

The diameter of the restrictor orifice exerts a pronounced influence on the load-carrying performance and film stiffness of the spherical hybrid bearing, exhibiting clear nonlinear characteristics.

As illustrated in Figures 18 and 19, the numerical evaluations reveal the impact of varying orifice diameters on load capacity. As the orifice diameter increases, both the axial and radial load capacities initially rise and then decline, indicating the existence of an optimal diameter range that maximises the bearing load. This behaviour can be attributed to the increased supply flow rate and strengthened hydrostatic effect resulting from a larger orifice. However, when the diameter becomes excessively large, the throttling effect weakens, leading to insufficient pressure being built up in the oil film and subsequent decrease in load capacity.

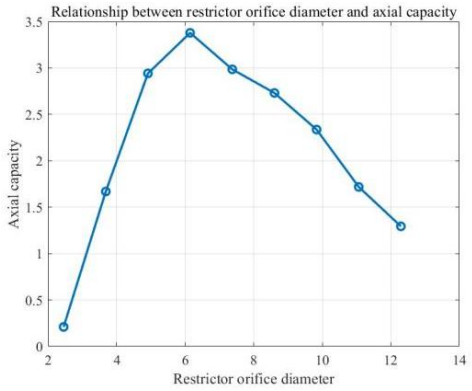

Figure 18. Relationship between Restrictor Orifice Diameter and Axial Capacity

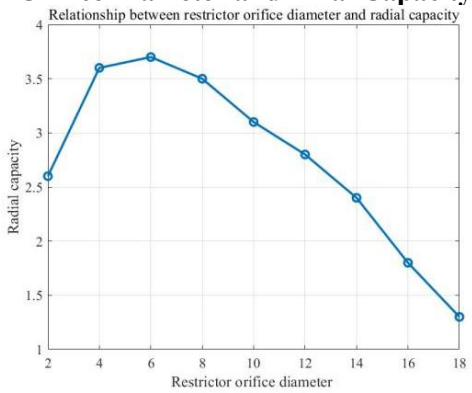

Figure 19. Relationship between Restrictor Orifice Diameter and Radial Capacity

Figures 20 and 21 illustrate the influence of the orifice diameter on stiffness. The axial stiffness also exhibits a "rise-and-fall" trend, reaching its maximum near the optimal orifice diameter. Conversely, the radial stiffness exhibited an upward trend in relation to the orifice diameter, signifying that the radial film stiffness is more substantially influenced by the augmented flow rate. The selection of the restrictor-orifice diameter must be made with consideration of the throttling pressure drop and the oil-film flow rate, in order to achieve optimal static performance in terms of load capacity and stiffness

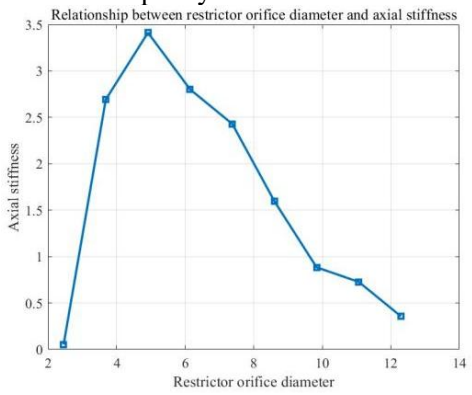

Figure 20. Relationship between Restrictor Orifice Diameter and Axial Stiffness

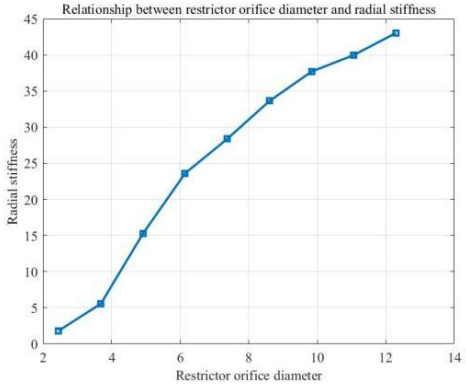

Figure 21. Relationship between Restrictor Orifice Diameter and Radial Stiffness

6. Conclusions

The present study systematically investigates the static characteristics of SHSBs utilised in roundness testers through numerical modelling and parametric analysis. The establishment of a spherical-coordinate lubrication model was achieved through the transformation of the Reynolds equation via the use of conformal mapping, thus facilitating the acquisition of the oil-film pressure distribution through the integration of the flow-continuity condition with a capillary-orifice restrictor model. The governing equations were solved using a finite-difference relaxation scheme, enabling quantitative evaluation of load capacity and stiffness under various operating and structural parameters. The primary conclusions that can be drawn from this analysis are as follows:

(1) A reliable numerical framework for SHSBs was developed by unfolding the hemispherical lubrication domain onto a rectangular plane and applying appropriate boundary conditions. The proposed model has been demonstrated to effectively capture the coupled hydrostatic–hydrodynamic lubrication behaviour, thereby providing stable convergence for pressure-field computation.

(2) The oil-film pressure distribution demonstrates significant local peaks in proximity to the restrictor orifices, which rapidly decay towards the surrounding regions. It has been demonstrated that an increase in supply pressure has a significant effect on the overall pressure level, thereby enhancing both axial and radial load-carrying capacities and film stiffness.

(3) It is imperative to acknowledge the pivotal function of bearing eccentricity in optimising static performance. Increased circumferential and axial eccentricities have been shown to strengthen the hydrodynamic effect, leading to

substantial improvements in load capacity and stiffness. When the eccentricity is minimal, the load capacity is constrained, signifying that a specific degree of eccentricity is requisite to achieve optimal utilisation of the hybrid lubrication mechanism.

(4) The initial oil-film clearance exerts a significant influence on the performance of the bearing. It has been demonstrated that larger eccentricities, when combined with appropriate film thicknesses, result in higher load capacity and stiffness. Conversely, excessively large clearances have been shown to have a detrimental effect on these parameters.

(5) The diameter of the restrictor-orifice has been demonstrated to manifest a discernible non-linear effect on the performance of the bearing. Initially, both axial and radial load capacities exhibit an increase, subsequently decreasing with increasing orifice diameter. This phenomenon unveils the existence of an optimal diameter range. This behaviour is the result of a balance between throttling pressure drop and lubricant flow rate. Axial stiffness exhibited a comparable trend, while radial stiffness demonstrated a general increase with orifice diameter.

The results obtained provide valuable insights into the parameter-dependent static behaviour of SHSBs. The proposed modelling approach and the identified performance trends offer practical guidance for the structural design and parameter optimisation of precision bearings in roundness testers and other ultra-precision rotating systems. Subsequent research will extend the present study to dynamic characteristics, thermal effects, and elastic deformation of bearing components, with a view to further improving model fidelity and engineering applicability.

Acknowledgments

This paper is supported by National Natural Science Foundation of China (No. 52305207).

References

[1] LI Yongming. Ultra-high precision hydrostatic ball bearing system. Acta Metrologica, 1986, (3):199-203.

[2] Xia Huan, Wang Yang, Tao Jizhong. Static Characteristics Analysis and Experimental Research on Aerostatic Spherical Bearings. Manufacturing Technology & Machine Tool, 2010, (03):20-24.

[3] Zha Shihong, Mei Tao. Numerical Calculation Method for a 6-DOF Simulated Satellite with Aerostatic Bearings. Robot, 2009, 31(06):561-567.

[4] Zhang Ke, Liu Dapeng. Numerical Analysis of Operating Characteristics of Aerostatic Spherical Gas Bearings. Lubrication Engineering, 2024, 49(06):169-176.

[5] Cui H, Xia H, Lei D, et al. A Calculation Method to Investigate the Effects of Geometric Parameters and Operational Conditions on the Static Characteristics of Aerostatic Spherical Bearings. Journal of Tribology, 2019, 141(2).

[6] Jia Chenhui, Gao Jing, Qiu Ming, et al. Analysis of Steady-State Load Capacity of Hemispherical Aerostatic Bearings. Bearing, 2018, (01):23-28+33.

[7] Li Zheng, Chen Qing, Wang Qunjing. Research on the Performance of Spherical Bearings Considering Cavitation Effect. Bearing, 2019, (09):28-35.

[8] Goenka P K, Booker J F. Spherical Bearings: Static and Dynamic Analysis Via the Finite Element Method. Journal of Lubrication Technology, 1980, 102(3):308-18.

[9] Meyer D. Reynolds Equation for Spherical Bearings. Journal of Tribology, 2002, 125(1):203-6.

[10] Zhen-bei L. Centrifugal inertia effects of the fluid flow between stepped spherical surfaces. Applied Mathematics and Mechanics, 1994, 15(2):175-87.

[11] Wang Jian, Shen Jingfeng. Analysis of Load-Carrying Characteristics of Hybrid Hydrostatic/Hydrodynamic Spherical Bearings Based on CFD. Journal of Mechanical Strength, 2021, 43(02):373-380.

[12] Wang Zhicheng, Xu Binggen. Analysis of Load Capacity in Spherical Hydrodynamic Sliding Bearings. Journal of Shanghai Institute of Mechanical Engineering, 1992, (03):60-70.

[13] Huang Ping. Numerical Calculation Methods in Lubrication. Beijing: Higher Education Press, 2012:12-32.

